LETTERS
https://doi.org/10.1038/s41563-019-0454-9

nature materials

Spin chirality fluctuation in two-dimensional ferromagnets with perpendicular magnetic anisotropy

Wenbo Wang[1,7], Matthew W. Daniels[2,3,7], Zhaoliang Liao[4,5,7], Yifan Zhao[6], Jun Wang[5], Gertjan Koster[5], Guus Rijnders[5], Cui-Zu Chang[6], Di Xiao[3] and Weida Wu[1*]

Non-coplanar spin textures with scalar spin chirality can generate an effective magnetic field that deflects the motion of charge carriers, resulting in a topological Hall effect (THE)[1–3]. However, spin chirality fluctuations in two-dimensional ferromagnets with perpendicular magnetic anisotropy have not been considered so far. Here, we report evidence of spin chirality fluctuations by probing the THE above the Curie temperature in two different ferromagnetic ultra-thin films, $SrRuO_3$ and V-doped Sb_2Te_3. The temperature, magnetic field, thickness and carrier-type dependence of the THE signal, along with Monte Carlo simulations, suggest that spin chirality fluctuations are a common phenomenon in two-dimensional ferromagnets with perpendicular magnetic anisotropy. Our results open a path for exploring spin chirality with topological Hall transport in two-dimensional magnets and beyond[4–7].

Understanding quantum transport of electrons in magnets is a fundamental issue in strongly correlated systems and spintronics[1–3]. If the magnetic moments form a non-coplanar spin texture as in many frustrated and/or chiral magnets, an electron travelling through the system will experience an effective magnetic field originated from the real-space Berry phase as it hops along a loop of three neighbouring magnetic moments (called a triad)[2]. Thus, this effective field is proportional to the scalar spin chirality of the triad and gives rise to a transverse response known as the topological Hall effect (THE). The THE is distinguished from both the ordinary Hall effect (OHE), which requires the application of an external magnetic field, and the anomalous Hall effect (AHE) found in ferromagnets with a uniform magnetization, in which the dominant contribution comes from the Berry phase in the momentum space in moderately conducting samples[8]. Because of its close relation to non-coplanar spin textures, the THE is a powerful probe to detect unconventional magnetic orders[7]. Indeed, the THE has been instrumental in the electric detection of skyrmion phase in chiral magnets and heterostructures[3,9–11].

While the THE is often interpreted as a signature of static spin textures with spin chirality in two-dimensional (2D) magnetic thin films, it has been proposed that thermal fluctuations of topological excitations could also result in a substantial Hall effect in three-dimensional magnets such as manganites[12–14]. However, the temperature dependence of the observed Hall resistivity cannot exclude the conventional mechanisms[2]. Herein, we report evidence of spin chirality fluctuation in 2D ferromagnets with perpendicular magnetic anisotropy (PMA) by probing the THE. A substantial THE signal was observed above the ferromagnetic transition temperatures T_c in two different itinerant ferromagnets, $SrRuO_3$ (SRO) and V (5%)-doped Sb_2Te_3 (VST) thin films in the 2D limit. The persistence of THE in the paramagnetic phase suggests a thermal-fluctuation origin. SRO is a metallic ferromagnet with n-type carriers[15], while VST is a magnetically doped topological insulator with p-type carriers[16]. The temperature (T), magnetic field (H), thickness (t) and carrier-type dependence of the THE are in agreement with our Monte Carlo (MC) simulations, supporting our assertion of spin chirality fluctuations in 2D ferromagnets with PMA. Given the existence of chiral spin orders and fluctuations in correlated systems, our finding opens the door to exploring the spin chirality with topological Hall transport in 2D ferromagnets[4–6] or quantum spin liquids[1,7].

The SRO thin films were grown on $SrTiO_3$ (STO) (001) substrates using pulsed laser deposition, while the VST films were grown on STO (111) substrates with molecular beam epitaxy (see Methods and Supplementary section A) We first focus on SRO films to illustrate the chiral-fluctuation-driven THE. A cartoon schematic of the SRO thin film structure and device configuration is shown in Fig. 1a. Electric contacts were fabricated with wire bonding and silver paint. The STO capping layer helps to enhance the ferromagnetic ordering in the ultra-thin limit[17]. Metallic behaviour was observed in all STO capped SRO films with thickness $t \geq 3$ unit cells (u.c.), while the 2 u.c. film is a non-magnetic insulator (see Supplementary Fig. 2 for transport data). The Curie temperature T_c is characterized by the peak anomaly of the slope of the longitudinal resistance (dR_{xx}/dT)[15,18]. Thinner SRO films are more resistive with lower T_c, which is consistent with the effect of reduced dimensionality[15].

In general, there are three contributions to the Hall resistivity in a magnetic metal: the OHE proportional to H, the conventional AHE proportional to the magnetization M and the THE due to the real-space Berry phase[3,10,11]. Therefore, we can express the Hall resistivity as

$$\rho_{yx}(H) = R_0 H + R_S M + \rho_{yx}^T \quad (1)$$

where R_0 is the OHE coefficient, R_S is the conventional AHE coefficient, and ρ_{yx}^T is the THE contribution. Here we will focus on the anomalous part, $\tilde{\rho}_{yx} \equiv \rho_{yx} - R_0 H$, by removing the OHE contribution. Well below T_c, a hysteresis loop of $\tilde{\rho}_{yx}$ was observed for all SRO

[1]Department of Physics and Astronomy, Rutgers University, Piscataway, NJ, USA. [2]Institute for Research in Electronics and Applied Physics, University of Maryland, College Park, MD, USA. [3]Department of Physics, Carnegie Mellon University, Pittsburgh, PA, USA. [4]National Synchrotron Radiation Laboratory, University of Science and Technology of China, Hefei, Anhui, China. [5]MESA+ Institute for Nanotechnology, University of Twente, Enschede, the Netherlands. [6]Department of Physics, Pennsylvania State University, University Park, PA, USA. [7]These authors contributed equally: Wenbo Wang, Matthew W. Daniels, Zhaoliang Liao. *e-mail: wdwu@physics.rutgers.edu

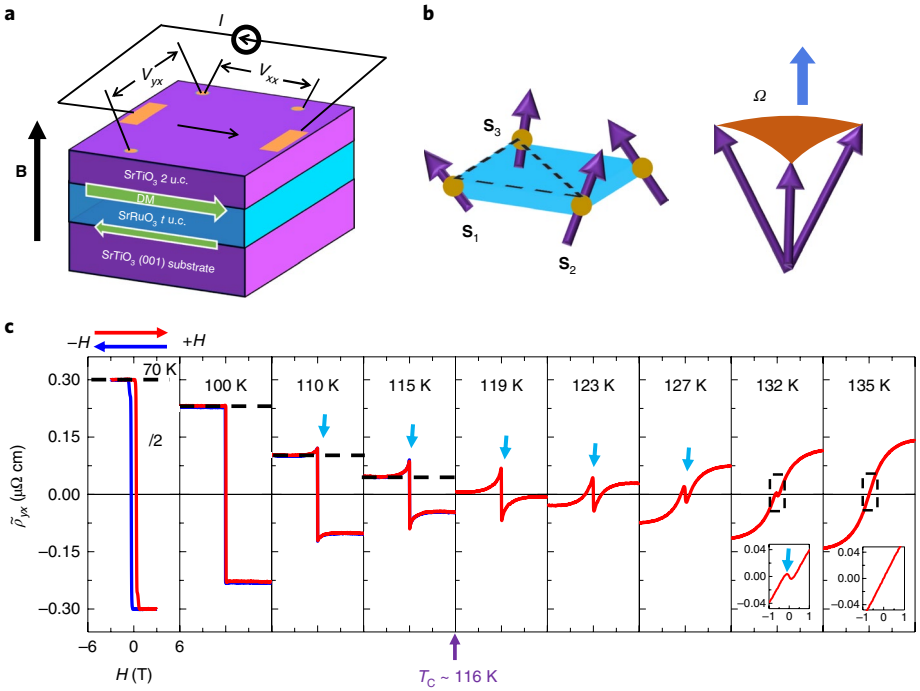

Fig. 1 | Scalar spin chirality and topological Hall effect in $SrRuO_3$ film. a, A schematic of *t* u.c. SRO film capped with 2 u.c. STO with electric contacts (orange patches) for transport measurements. The $(STO)_2/(SRO)_t$ bilayers are grown on STO (001) substrates. *t* is the thickness of the SRO film. A current (*I*) was passed through the film and longitudinal (V_{xx}) and transverse (V_{yx}) voltages were measured simultaneously. The Dzyaloshinsky–Moriya (DM) vectors (green arrows) on the two interfaces point in opposite directions. **b**, a snapshot of neighbouring non-coplanar spins on a square lattice (cyan). S_1, S_2 and S_3 are three neighbouring spins (purple arrows) of the Ru atoms (yellow spheres) in SRO films. These three non-coplanar spins subtend a solid angle Ω, resulting in an effective magnetic field (blue arrow). **c**, the Hall resistivity $\tilde{\rho}_{yx}$ of SRO film (6 u.c.) with OHE subtracted as a function of magnetic field *H* at various temperatures from 100 K to 135 K. Blue (red) curves were taken as the magnetic field from −6 to 6 T (6 to −6 T). The cyan arrows indicate the THE humps emerge above 100 K. The insets show enlarged curves of 132 and 135 K data around zero field, suggesting THE peaks are absent above 135 K.

(and VST) films (see Supplementary sections I–K). This loop has the same shape as the magnetization hysteresis loop, indicating that below T_c the main contribution to $\tilde{\rho}_{yx}$ comes from the conventional AHE ($\propto M$). This is similar to previous reports of $\tilde{\rho}_{yx}$ on magnetic thin films with PMA[16,19–21].

Surprisingly, at higher temperatures a sharp anomaly in $\tilde{\rho}_{yx}(H)$ develops around T_c. Figure 1c shows $\tilde{\rho}_{yx}(H)$ of the STO-capped SRO film (6 u.c.). Below $T_c \approx 116$ K, $\tilde{\rho}_{yx}(H)$ shows a pronounced square shape, indicating a robust ferromagnetic ordering with a strong uniaxial anisotropy[15]. As *T* approaches T_c, a prominent antisymmetric peak near zero field emerges. This emergent feature indicates an additional contribution to the Hall signal, which we attribute to the THE. In particular, the AHE changes its sign around 119 K as evidenced from the high-field values of $\tilde{\rho}_{yx}(H)$. This is due to the strong energy dependence of the AHE near the Fermi energy[22]. Therefore, $\tilde{\rho}_{yx}(H)$ data at 119 K are dominated by the THE signal (see Supplementary section I.4 for the complete dataset). The THE data at 119 K are different from the conventional AHE, showing a sharp antisymmetric peak near zero field followed by a smooth suppression at high fields. Furthermore, this antisymmetric peak feature becomes strongest slightly above T_c, then gradually decreases and disappears around 132 K, well into the paramagnetic phase. Note that the THE feature is visible in the raw Hall data (see Supplementary section C). The persistence of THE in the paramagnetic phase above T_c demonstrates a thermally driven spin chirality fluctuation mechanism[23,24], which is distinct from the THE due to static spin texture emerging below T_c in previous studies[19–21].

To extract the *T* evolution of the THE signal, the AHE contribution ($\propto M$) at each *T* needs to be properly subtracted. It is technically challenging to directly measure the uniform out-of-plane magnetization of thin films in the 2D limit because of diminishing stray field due to the demagnetization factor[25]. For our SRO films, the $M(H)$ curves of the paramagnetic phase ($T > T_c$) can be described by a Langevin function (or self-consistent equation using a Brillouin function, see Supplementary section D). Since the the antisymmetric peak feature becomes negligible for $T \geq 135$ K, these high-temperature AHE data are used for the Langevin fitting. For $T < T_c$, a step function is used to approximate the AHE contribution. Figure 2 shows an example of AHE background subtraction. The raw data $\rho_{yx}(H)$ at 127 K are shown in Fig. 2a. The negative slope at high field indicates n-type charge carriers[15]. Figure 2b shows $\tilde{\rho}_{yx}(H)$ after removing the OHE and the Langevin fitting of the AHE background. The difference (green area) between them is the THE signal ρ_{yx}^T, which is plotted in Fig. 2c. Using this procedure, we extracted ρ_{yx}^T of the 6 u.c. SRO film at various *T* as shown in Fig. 2d. The antisymmetric THE peaks are visible from 110 K to 132 K and are most pronounced around T_c, which suggests that the observed THE originates from the thermal fluctuation of spin chirality.

Similar T–H dependence of THE was also observed in thinner STO-capped SRO films with $t = 3, 4, 5$, consistent with a THE induced by spin chirality fluctuations (see Supplementary sections I and J). Furthermore, the THE is absent in thicker SRO films ($t > 7$), supporting the 2D nature of the spin chirality fluctuation due to the spatial confinement effect. Figure 3a shows the maximum values of ρ_{yx}^T as a function of reduced temperature T/T_c. The THE signal peaks around T_c, then diminishes approximately 20% above T_c. The non-monotonic thickness dependence of the THE magnitudes might come from the combined effects of the effective exchange (*J*) and other parameters (for example, anisotropy, magnetic dis-

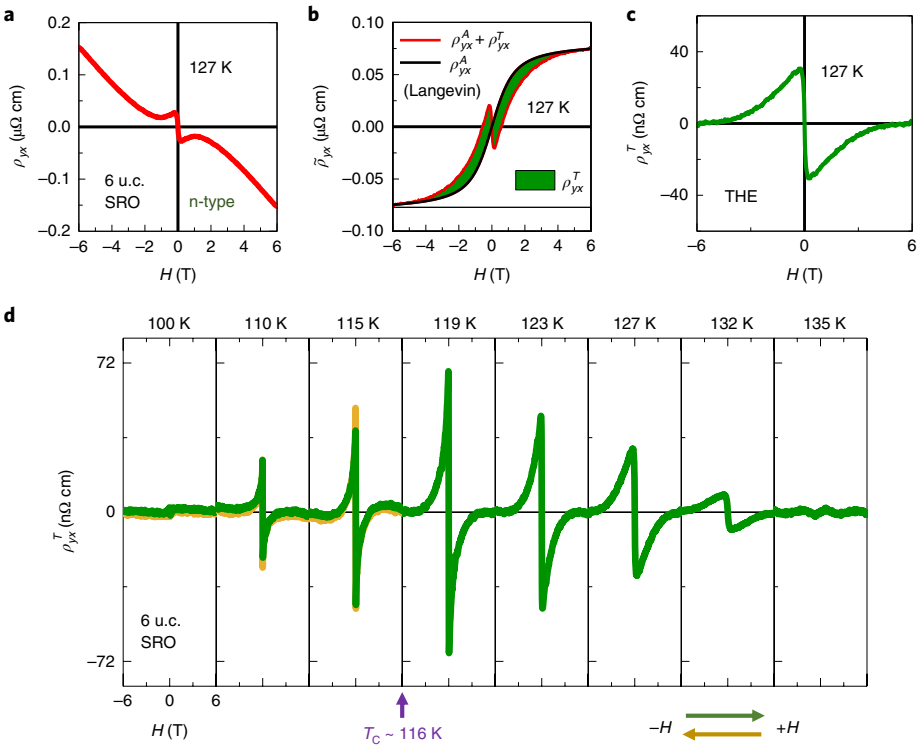

Fig. 2 | Extracting the THE signal (ρ_{yx}^T) in SRO films. a, Raw data ρ_{yx} of SRO film (6 u.c.) at 127 K. The negative slope at high field indicate n-type carriers. **b**, $\tilde{\rho}_{yx}$ (black) of the SRO film at 127 K was fitted with a Langevin function (red). The green area is the THE signal, which is plotted in **c**. **d**, ρ_{yx}^T of SRO film as a function of magnetic field H at various temperature from 100 K to 135 K. Green (yellow) curves are taken as the magnetic field from −6 to 6 T (6 to −6 T). The Curie temperature T_c ~ 116 K is indicated by the purple arrow.

orders). The qualitative T–H dependences of the THE signal are consistent with the prior theoretical studies of thermal fluctuations in 2D chiral magnets[23,24]. However, spin chirality fluctuations in 2D ferromagnets with strong PMA have not been addressed.

To gain insight into the emergent spin chirality fluctuation in 2D ferromagnets with PMA, we carried out MC simulations with the following Hamiltonian (see Methods and Supplementary section N for details):

$$H = \sum_{\langle ij \rangle} [-J(\mathbf{S}_i \cdot \mathbf{S}_j) + \mathbf{D}_{ij} \cdot (\mathbf{S}_i \times \mathbf{S}_j)] - K \sum_i (S_i^z)^2 - B_z \sum_i S_i^z$$

where $\mathbf{S}_i = S\mathbf{n}_i$ is the spin on the ith lattice site. The first term ($J > 0$) describes ferromagnetic Heisenberg exchange coupling. The second term describes the chiral interaction, namely the Dzyaloshinsky–Moriya interaction (DMI)[26,27], arising from the inversion symmetry breaking (due to interfaces, for example). The uniaxial anisotropy K is included in the third term. With $D < D_c \equiv 2\sqrt{2JK}/\pi$ (D_c is the critical DMI value that separates uniform ferromagnet and chiral magnet ground states), the ground state is a ferromagnet with uniform out-of-plane (OOP) magnetization despite of the presence of DMI[28]. The last term is the Zeeman energy due to the external magnetic field B_z.

It appears that the DMI is forbidden by the symmetric structure (STO/SRO/STO) of our films. However, it has been shown that the STO film grown on SRO is slightly different from the STO substrate[29]. This slight difference breaks the OOP inversion symmetry, allowing a small but non-zero chiral interaction (DMI). Thus, non-zero spin chirality emerges when the ferromagnetic order is 'melted' by thermal fluctuations around T_c. The emergent spin chirality is characterized by the topological charge Q defined as:

$$Q = \frac{1}{4\pi} \int \mathrm{d}^2\mathbf{r}\, [\mathbf{n} \cdot (\partial_x \mathbf{n} \times \partial_y \mathbf{n})] \qquad (2)$$

where $\mathbf{n}$ is a unit vector describing the local spin direction. On a lattice, the integral is replaced by the sum of the solid angle Ω subtended by three neighbouring spins (a triad) as shown in Fig. 1b[30]. As shown in Fig. 3b, our MC simulations demonstrate that the topological charge density $Q(H)$ is non-zero around T_c, showing qualitatively the same antisymmetric peak structure as that of the observed THE (see Supplementary section N). The agreement suggests that the observed THE originates from the effective magnetic field generated by the thermal-fluctuation-driven spin chirality.

The H dependence of the THE can be understood in the following physical picture. At the limit of $H \to 0$, the induced Q is proportional to H because each triad carries a net moment as shown in Fig. 3b. Therefore, $Q \propto H \propto M$ in the paramagnetic phase at $H \to 0$. At the high-field limit ($H \to \infty$), the Zeeman energy competes with the DMI, thus suppressing the solid angles Ω of all triads, resulting in a vanishing Q (and THE). The leading order in the high-field expansion is proportional to D^2 because Q respects the spatial inversion symmetry[23], so $Q \propto (D/H)^2$ as demonstrated by the cyan line in Fig. 3b. Thus, the overall H dependence can be described by a phenomenological function that interpolate these two limits:

$$Q(H) \propto \frac{M(H)}{1 + (H/D_{\mathrm{eff}})^2} \qquad (3)$$

where D_{eff} is the effective DMI. This function reasonably describes both MC simulations and experimental data, supporting the simple intuitive picture (see Supplementary section L for detailed analysis). As shown in Fig. 3c, the width of THE peak decreases systematically as t increases, indicating decreasing D_{eff}. This behaviour is also supported by our MC simulations with varying DMI (see Supplementary section L). Using equation (3), we extracted the values of D_{eff} (up to a numerical factor) of the STO-capped (3, 4, 5 and

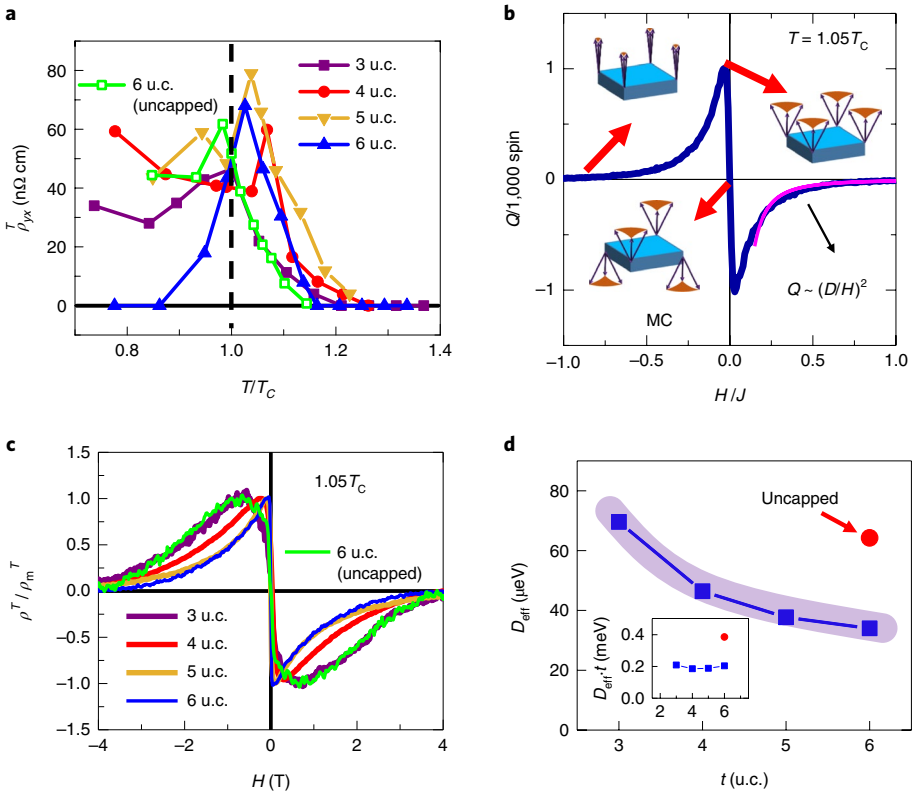

Fig. 3 | *T*–*H* dependence of THE (ρ_{yx}^T) in SRO films and the effective DMIs (D_{eff}). a, Maximum values of ρ_{yx}^T as a function of temperature T of SRO films with thickness $t = 3$–6 u.c. capped with STO and the 6 u.c. uncapped SRO film. **b**, MC simulations (uniaxial anisotropy $K = 0.5J$ and DMIs $D = 0.25J < D_c$) of topological charges Q at $T = 1.05T_c$ show an antisymmetric profile similar to the experimental data of THE. The high-field tail can be described by $(D/H)^2$ (the magenta curve). The inset cartoons show the behaviour of spin triads at various magnetic fields, as indicated by the red arrows. **c**, H dependence of normalized ρ_{yx}^T at the reduced temperature $1.05T_c$. ρ_m^T is the maximum THE signal. The 6 u.c. uncapped SRO film is indicated by the green curve. **d**, t dependence of effective DMIs (D_{eff}). The D_{eff} was extracted from fitting the H dependence of ρ_{yx}^T shown in **c**. The 6 u.c. uncapped SRO film is indicated by the red circle. The inset shows that the product $D_{eff} \times t$ is approximately a constant, suggesting an interface origin.

6 u.c.) and uncapped (6 u.c.) SRO films. $D_{eff} \times t$ values are shown in the inset of Fig. 3d. Essentially D_{eff} of the STO-capped films is inversely proportional to t, in agreement with the interface origin of D_{eff}. Furthermore, the D_{eff} of uncapped SRO film (6 u.c.) is about twice as large as that of the capped one, which is consistent with the stronger inversion symmetry breaking of the uncapped SRO film. The estimated interface DMI value is $D \approx 0.2$ meV, which is approximately one to two orders of magnitude smaller than that of the $SrIrO_3$/SRO interface[20], in good agreement with the expectation of weak DMI in our SRO films.

To demonstrate the common nature of spin chirality fluctuation, we present Hall data of five-quintuple (QL) VST thin film capped with three-QL Sb_2Te_3 (ST). Because the carrier density of our ST/VST film is approximately 1,000 times smaller than that of SRO, the Fermi level of the ST/VST film can be shifted substantially by a gate voltage. More interestingly, the AHE can be tuned to zero at every T, which allows an unambiguous isolation of the THE signal. The schematic of the heterostructure is shown in Fig. 4a. Figure 4b shows the raw data (ρ_{yx}) of the ST/VST film. The positive slope at high field indicates p-type carriers. An example of gate tuning AHE at 30 K is shown in Fig. 4c (see Supplementary section K for the complete dataset). Figure 4d shows the THE data at T above and below $T_c \approx 27.5$ K, showing qualitatively the same T–H dependences as that of SRO films. Furthermore, the sign of the THE is consistent with that of the carrier type, in agreement with the same effective magnetic field due to the same spin chirality fluctuations in these two different 2D ferromagnets with PMA.

This agreement suggests that the THE observed in SRO and VST films originates from the 2D spin chirality fluctuations. For $T > T_c$, the suppression of the THE signal approximately follows a power law, in reasonable agreement with that of MC simulations (see Supplementary section M). This would inspire future studies of the critical scaling behaviour of the spin chirality fluctuation. Although the ground states of both systems are simple ferromagnets where the static skyrmion phase is unstable because $D \ll D_c$, the thermal fluctuations around T_c are chiral due to the presence of the (weak) chiral interaction D. How D influences the critical behaviour of 2D ferromagnets with PMA is an interesting subject to explore in future studies.

Although the THE diminishes at $T \ll T_c$ in STO-capped 6 u.c. SRO film, the THE persists to low temperatures in the 3 u.c. SRO film and the ST/VST film (see Supplementary sections I and K). It is unclear whether the low-temperature THE originates from static topological spin texture (for example, skrymions), which will inspire future studies of the THE in Berry phase engineered magnetic thin films such as the ST/VST films. Our report of spin chirality fluctuations opens the door to further exploration of topological Hall transport in other itinerant 2D ferromagnets and beyond[4–6], and may help to identify chiral spin liquid states with quantum entanglements in 2D correlated systems using topological Hall transport[1,7].

Online content

Any methods, additional references, Nature Research reporting summaries, source data, statements of code and data availability and

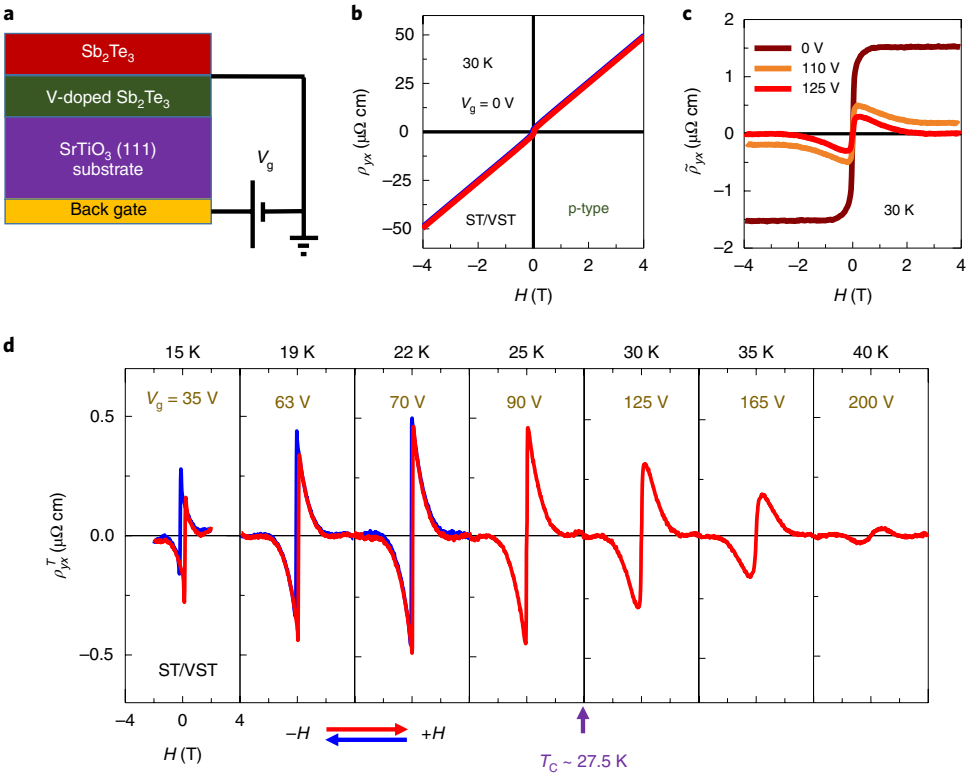

Fig. 4 | THE (ρ_{yx}^{T}) of ST-capped VST films. a, A schematic of the $(ST)_3/(VST)_5$ heterostructure grown on STO (111) substrate. A back-gate voltage (V_g) was applied to tune the AHE. **b**, Raw data ρ_{yx} of ST/VST film at 30 K. The positive slope at high field indicates p-type carriers. **c**, $\tilde{\rho}_{yx}$ of VST film at 30 K with different gate voltages. The AHE is tuned to zero at 125 V so that only THE is visible. **d**, ρ_{yx}^{T} of VST film as a function of magnetic field H at various temperature from 15 K to 40 K. Red (blue) curves were taken as the magnetic field from −6 to 6 T (6 to −6 T). The Curie temperature T_c ~ 27.5 K is indicated by the purple arrow. The overall behaviour is qualitatively the same as that of SRO films.

associated accession codes are available at https://doi.org/10.1038/s41563-019-0454-9.

Received: 28 November 2018; Accepted: 9 July 2019;
Published online: 12 August 2019

References

1. Wen, X. G., Wilczek, F. & Zee, A. Chiral spin states and superconductivity. *Phys. Rev. B* **39**, 11413–11423 (1989).
2. Taguchi, Y., Oohara, Y., Yoshizawa, H., Nagaosa, N. & Tokura, Y. Spin chirality, Berry phase, and anomalous Hall effect in a frustrated ferromagnet. *Science* **291**, 2573–2576 (2001).
3. Neubauer, A. et al. Topological Hall effect in the A phase of MnSi. *Phys. Rev. Lett.* **102**, 186602 (2009).
4. Bonilla, M. et al. Strong room-temperature ferromagnetism in VSe_2 monolayers on van der Waals substrates. *Nat. Nanotechnol.* **13**, 289–293 (2018).
5. Fei, Z. et al. Two-dimensional itinerant ferromagnetism in atomically thin Fe_3GeTe_2. *Nat. Mater.* **17**, 778–782 (2018).
6. Deng, Y. J. et al. Gate-tunable room-temperature ferromagnetism in two-dimensional Fe_3GeTe_2. *Nature* **563**, 94–99 (2018).
7. Machida, Y., Nakatsuji, S., Onoda, S., Tayama, T. & Sakakibara, T. Time-reversal symmetry breaking and spontaneous Hall effect without magnetic dipole order. *Nature* **463**, 210–213 (2010).
8. Nagaosa, N., Sinova, J., Onoda, S., MacDonald, A. H. & Ong, N. P. Anomalous Hall effect. *Rev. Mod. Phys.* **82**, 1539–1592 (2010).
9. Zang, J., Mostovoy, M., Han, J. H. & Nagaosa, N. Dynamics of Skyrmion crystals in metallic thin films. *Phys. Rev. Lett.* **107**, 136804 (2011).
10. Kanazawa, N. et al. Large topological hall effect in a short-period helimagnet MnGe. *Phys. Rev. Lett.* **106**, 156603 (2011).
11. Huang, S. X. & Chien, C. L. Extended skyrmion phase in epitaxial FeGe(111) thin films. *Phys. Rev. Lett.* **108**, 267201 (2012).
12. Matl, P. et al. Hall effect of the colossal magnetoresistance manganite $La_{1-x}Ca_xMnO_3$. *Phys. Rev. B* **57**, 10248–10251 (1998).
13. Ye, J. W. et al. Berry phase theory of the anomalous Hall effect: application to colossal magnetoresistance manganites. *Phys. Rev. Lett.* **83**, 3737–3740 (1999).
14. Chun, S. H., Salamon, M. B., Lyanda-Geller, Y., Goldbart, P. M. & Han, P. D. Magnetotransport in manganites and the role of quantal phases: theory and experiment. *Phys. Rev. Lett.* **84**, 757–760 (2000).
15. Koster, G. et al. Structure, physical properties, and applications of $SrRuO_3$ thin films. *Rev. Mod. Phys.* **84**, 253–298 (2012).
16. Chang, C.-Z. et al. High-precision realization of robust quantum anomalous Hall state in a hard ferromagnetic topological insulator. *Nat. Mater.* **14**, 473–477 (2015).
17. Thomas, S. et al. Localized control of Curie temperature in perovskite oxide film by capping-layer-induced octahedral distortion. *Phys. Rev. Lett.* **119**, 177203 (2017).
18. Klein, L. et al. Transport and magnetization in the badly metallic itinerant ferromagnet $SrRuO_3$. *J. Phys. Condens. Matter* **8**, 10111–10126 (1996).
19. Yasuda, K. et al. Geometric Hall effects in topological insulator heterostructures. *Nat. Phys.* **12**, 555–559 (2016).
20. Matsuno, J. et al. Interface-driven topological Hall effect in $SrRuO_3$-$SrIrO_3$ bilayer. *Science Adv.* **2**, e1600304 (2016).
21. Liu, C. et al. Dimensional crossover-induced topological Hall effect in a magnetic topological insulator. *Phys. Rev. Lett.* **119**, 176809 (2017).
22. Fang, Z. et al. The anomalous Hall effect and magnetic monopoles in momentum space. *Science* **302**, 92–96 (2003).
23. Hou, W.-T., Yu, J.-X., Daly, M. & Zang, J. Thermal driven topology in chiral magnets. *Phys. Rev. B* **96**, 140403(R) (2017).
24. Böttcher, M., Heinze, S., Egorov, S., Sinova, J. & Dupe, B. B-T phase diagram of Pd/Fe/Ir(111) computed with parallel tempering Monte Carlo. *New J. Phys.* **20**, 103014 (2018).
25. Hellwig, O., Berger, A., Kortright, J. B. & Fullerton, E. E. Domain structure and magnetization reversal of antiferromagnetically coupled perpendicular anisotropy films. *J. Mag. Mag. Mater.* **319**, 13–55 (2007).
26. Dzyaloshinsky, I. A thermodynamic theory of 'weak' ferromagnetism of antiferromagnetics. *J. Phys. Chem. Solids* **4**, 241–255 (1958).
27. Moriya, T. Anisotropic superexchange interaction and weak ferromagnetism. *Phys. Rev.* **120**, 91–98 (1960).
28. Rohart, S. & Thiaville, A. Skyrmion confinement in ultrathin film nanostructures in the presence of Dzyaloshinskii–Moriya interaction. *Phys. Rev. B* **88**, 184422 (2013).

29. Hyun, S. & Char, K. Effects of strain on the dielectric properties of tunable dielectric $SrTiO_3$ thin films. *Appl. Phys. Lett.* **79**, 254 (2001).
30. Berg, B. & Luescher, M. Definition and statistical distributions of a topological number in the lattice O(3) σ-model. *Nucl. Phys. B* **190**, 412–424 (1981).

Acknowledgements

We are grateful to R. Swendsen for many useful discussions on MC simulations. The work at Rutgers was supported by the Office of Basic Energy Sciences, Division of Materials Sciences and Engineering, US Department of Energy under award no. DE-SC0018153. The work at CMU was supported by the Office of Basic Energy Sciences, Division of Materials Sciences and Engineering, US Department of Energy under award no. DE-SC0012509. The work at UMD was supported under the Cooperative Research Agreement between the University of Maryland and the National Institute of Standards and Technology Center for Nanoscale Science and Technology, award no. 70NANB14H209, through the University of Maryland. The work at U. Twente was supported by Nederlandse Organisatie voor Wetenschappelijk Onderzoek through grant no. 13HTSM01. The work at Penn State was supported by ARO Young Investigator Program award no. W911NF1810198. C.-Z.C. acknowledges support of an Alfred P. Sloan Research Fellowship.

Author contributions

W.Wu conceived and supervised the project. Z.L., J.W., G.K. and G.R. synthesized the SRO samples and performed X-ray diffraction. Y.Z. and C.-Z.C. synthesized the VST samples. W.Wang performed the magnetotransport experiments and analysed the data. M.W.D. and D.X. performed the MC simulations. W.Wang, W.Wu, M.W.D. and D.X. wrote the manuscript. All authors discussed the data and contributed to the manuscript.

Competing interests

The authors declare no competing interests.

Additional information

Supplementary information is available for this paper at https://doi.org/10.1038/s41563-019-0454-9.

Reprints and permissions information is available at www.nature.com/reprints.

Correspondence and requests for materials should be addressed to W.W.

Publisher's note: Springer Nature remains neutral with regard to jurisdictional claims in published maps and institutional affiliations.

Methods

Sample growth and characterization. Both SRO and STO layers were epitaxially grown on TiO_2-terminated (001) STO substrates using a pulsed laser deposition technique. The single TiO_2-terminated STO substrates were achieved by standard buffer hydrofluoric acid (HF) etching for 30 s and subsequent annealing at 950 °C for 90 min. During the growth of either SRO or STO, the laser fluence and repetition rate were 2 J cm^{-2} and 1 Hz, respectively. The substrate temperature and oxygen partial pressure during growth were 650 °C and 0.25 mbar, respectively. In-situ reflection high-energy electron diffraction was used to monitor the growth and confirmed a layer-by-layer growth fashion. All the films showed an atomic flat surface with similar terrace structure with substrates. X-ray diffraction was carried out using a PANalytical XPert Materials Research Diffractometer in high-resolution mode.

The $Sb_2Te_3/Sb_{2-x}V_xTe_3$ ($x=0.1$) heterostructure was grown on $SrTiO_3$(111) substrate with a molecular beam epitaxy (MBE) method. The insulating $SrTiO_3$ (111) substrates used for the growth were first soaked in 90 °C deionized water for 1.5 h, and then annealed at 985 °C for 3 h in a tube furnace with flowing pure oxygen gas. Through the above heat treatment, the STO (111) substrate surface become passivated and atomically flat; the topological insulator (TI) heterostructure growth was carried out using a commercial EPI-620 MBE system with a vacuum that was better than 2×10^{-10} mbar. The heat-treated insulating STO (111) substrates were outgassed at ~530 °C for 1 h before the growth of the TI heterostructures. High-purity Sb (99.999%) and Te (99.999%) were evaporated from Knudsen effusion cells and V (99.995%) was evaporated from an e-gun. During growth of the TI, the substrate was maintained at 240 °C. The flux ratio of Te to Sb was set to be >10 to prevent Te deficiency in the samples. The pure or magnetic TI growth rate was at ~0.25 QL min^{-1}. Following the growth, the TI films were annealed at ~240 °C for 30 min to improve the crystal quality before being cooled down to room temperature. Finally, to avoid possible contamination, an 18-nm-thick Te layer was deposited at room temperature on top of the sandwich heterostructures before their removal from the MBE chamber for transport measurements.

Transport measurements. The Hall resistance and longitudinal resistance were measured by standard lock-in techniques with an alternating current of 40 μA modulated at 314 Hz. All Hall data are antisymmetrized.

Monte Carlo simulations. The MC simulations were conducted on a $N^2=32\times32$ square lattice with periodic boundary conditions. The Hamiltonian was used as the energy function underlying the standard Metropolis algorithm. The expression of Ω is as follows:

$$\exp\left(\frac{i\Omega}{2}\right)=r^{-1}(1+\mathbf{S}_1\cdot\mathbf{S}_2+\mathbf{S}_2\cdot\mathbf{S}_3+\mathbf{S}_3\cdot\mathbf{S}_1+i\chi) \quad (4)$$

where $\chi\equiv\boldsymbol{S}_1\cdot(\boldsymbol{S}_2\times\boldsymbol{S}_3)$ is the spin chirality of the three neighbouring spins[1] and $r=\sqrt{2(1+\mathbf{S}_1\cdot\mathbf{S}_2)(1+\mathbf{S}_2\cdot\mathbf{S}_3)(1+\mathbf{S}_3\cdot\mathbf{S}_1)}$ is the normalization factor. The sign of chirality is fixed by the chiral interaction (DMI). The total topological charge Q is then given by summing Ω over all the right-handed spin triangles in the lattice,

$$Q=\frac{1}{4\pi}\sum_{\triangle ijk}\Omega(\mathbf{S}_i,\mathbf{S}_j,\mathbf{S}_k) \quad (5)$$

Q (or χ) is an odd function with respect to time reversal symmetry, so $Q(H)=-Q(-H)$. Thus, for the paramagnetic phase with $H=0$, the net topological charge is zero, $Q(0)=0$, corresponding to equal populations of 'up' and 'down' triads.

To illustrate chiral fluctuations, we present representative MC simulation results with parameters $D=0.25J$ and $K=0.5J$. The simulation of 32×32 sites shows a ferromagnetic ordering with $T_c\approx0.85J$. The extrapolated thermodynamic $T_c\approx0.71J$. At $T=J>T_c$, the $M(H)$ curve shows the expected paramagnetic behaviour without hysteresis.

Data availability

The data that support the findings of this study are available from the corresponding author upon reasonable request.

Code availability

The code for the MC simulations is available from M.W.D. and D.X. on reasonable request.